arXiv:1606.04179v1 [cond-mat.mtrl-sci] 14 Jun 2016

Optical Absorption Spectra and Excitons of Dye-Substrate Interfaces: Catechol on TiO_2(110)

Duncan John Mowbray*,† and Annapaola Migani*,‡

*Nano-Bio Spectroscopy Group and ETSF Scientific Development Center, Departamento de Física de Materiales, Universidad del País Vasco UPV/EHU and DIPC, E-20018 San Sebastián, Spain

‡Catalan Institute of Nanoscience and Nanotechnology (ICN2), CSIC and The Barcelona Institute of Science and Technology, Campus UAB, Bellaterra, E-08193 Barcelona, Spain

Supporting Information

ABSTRACT: Optimizing the photovoltaic efficiency of dye-sensitized solar cells (DSSC) based on staggered gap heterojunctions requires a detailed understanding of sub-band gap transitions in the visible from the dye directly to the substrate's conduction band (CB) (type-II DSSCs). Here, we calculate the optical absorption spectra and spatial distribution of bright excitons in the visible region for a prototypical DSSC, catechol on rutile TiO_2(110), as a function of coverage and deprotonation of the OH anchoring groups. This is accomplished by solving the Bethe-Salpeter equation (BSE) based on hybrid range-separated exchange and correlation functional (HSE06) density functional theory (DFT) calculations. Such a treatment is necessary to accurately describe the interfacial level alignment and the weakly bound charge transfer transitions that are the dominant absorption mechanism in type-II DSSCs. Our HSE06 BSE spectra agree semi-quantitatively with spectra measured for catechol on anatase TiO_2 nanoparticles. Our results suggest deprotonation of catechol's OH anchoring groups, while being nearly isoenergetic at high coverages, shifts the onset of the absorption spectra to lower energies, with a concomitant increase in photovoltaic efficiency. Further, the most relevant bright excitons in the visible region are rather intense charge transfer transitions with the electron and hole spatially separated in both the [110] and [001] directions. Such detailed information on the absorption spectra and excitons is only accessible via periodic models of the combined dye-substrate interface.

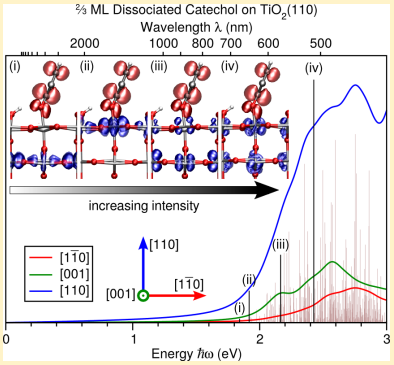

1. INTRODUCTION

Dye-sensitized solar cells (DSSCs) show great promise as sources of inexpensive, flexible, clean energy.[1] The photovoltaic efficiency of such a device is proportional to its absorption of the solar spectrum.[2] The introduction of the dye facilitates absorption within the visible region via sub-band gap transitions.[3,4] For DSSCs with staggered gap heterojunctions, this is via transitions from the highest occupied molecular orbital (HOMO) of the dye in the substrate's gap to the conduction band (CB).[5] In such DSSCs, an electron is excited either to the lowest unoccupied molecular orbital (LUMO) of the dye and relaxes to the conduction band minimum (CBM) of the substrate (type-I DSSC),[6−10] or to the CBM directly (type-II DSSC).[11−16] For type-I DSSCs, the device's photovoltaic efficiency is determined by the dye's energy gap and the interfacial level alignment of the LUMO and the CBM,[10] while for type-II DSSCs, the device's photovoltaic efficiency is determined by the interfacial level alignment of the HOMO and the CBM.[14] To determine which process dominates, one must consider the optical absorption of the isolated dye, substrate, and their interface.

A prototypical staggered gap heterojunction is the catechol–TiO_2 interface,[3,13−27] as catechol is a typical anchoring group for more complex organic and inorganic dyes,[5,12,13,28] and TiO_2 is a highly stable large gap semiconductor commonly used in staggered gap heterojunctions. Furthermore, for catechol-TiO_2 interfaces, other factors that reduce the device's photovoltaic efficiency, such as electron-hole recombination, binding and conductivity, are less relevant. For this reason, the photovoltaic efficiency of catechol–TiO_2 interfaces is mostly determined by the strength of the optical absorption in the visible region.

The level alignment of catechol overlayers on rutile TiO_2(110) has been studied experimentally via ultraviolet photoemission spectroscopy (UPS),[20,29] inverse photoemission spectroscopy (IPES),[29] and theoretically using density functional theory (DFT)[3,16,20−23,30] and quasiparticle (QP) techniques such as G_0W_0.[3,23] We have previously shown[23,31−35] that G_0W_0[36−38] calculations based on the PBE[39] exchange and correlation (xc)-functional reproduce the interfacial level alignment of molecular levels from UPS,[20,29,40−43] IPES,[29] and two-photon photoemission (2PP)[44] experiments. In so doing, we were able to verify the structure of catechol overlayers on the TiO_2(110) surface.[23]

However, to describe the efficiency of a photovoltaic device, one also needs to consider the intensity of absorption of the solar spectrum. Here, we calculate the optical absorption spectra and excitons of catechol–TiO_2(110) interfaces by solving the Bethe-Salpeter equation (BSE)[45,46] based on hybrid range-separated (HSE06)[47] xc-functional DFT calculations, using an isotropic screening of the electron-hole interaction ($\epsilon_\infty \approx 4$).[48,49]

Since catechol's intramolecular HOMO→LUMO transitions on TiO_2 are supra-band gap by more than 2 eV,[23] the only sub-band gap transitions are from the HOMO and HOMO−1 levels of the catechol overlayer[20,23] to the unoccupied Ti 3*d* levels with t_{2g}-like symmetry[50−52] of the substrate. These are charge transfer transitions,[15,17−19,27] which require a proper description of the long-

ranged electron-hole interaction,[53–56] as provided by hybrid xc-functionals.[48,49,57] It is the level alignment of these levels, and the distribution of their wave functions, which is most relevant for describing the optical absorption of the catechol–TiO_2(110) interface at the BSE level.

Our previous work has shown that G_0W_0 calculations significantly overestimate the electronic band gap of the TiO_2(110) surface by ~ 1 eV.[32] This makes the quasiparticle G_0W_0 eigenvalues of the catechol–TiO_2(110) interface a poor starting point for solving the Bethe-Salpeter equation. Conversely, the electronic band gap of the TiO_2(110) surface is described near quantitatively by DFT calculations based on the hybrid range-separated HSE06 xc-functional.[32] Furthermore, HSE06 DFT calculations provide Kohn-Sham (KS) wave functions in closer agreement to the many-body wave functions obtained via self-consistent quasiparticle *GW* (scQP*GW*) calculations.[31,32] This suggests HSE06 DFT may provide a better basis set for BSE calculations of absorption spectra. This is important, as we are restricting our electron-hole basis set to occupied HOMO and HOMO−1 levels and unoccupied levels less than 7 eV above in our BSE calculations.

We begin by providing the computational parameters employed in section 2.1, the terminology used in section 2.2, the procedure for aligning the density of states (DOS) in section 2.3, and the Bethe-Salpeter equation in section 2.4. For the most stable catechol overlayers on rutile TiO_2(110) we provide their structure and stability in section 3.1, interfacial level alignment in section 3.2, and sub-band gap optical absorption in section 3.3. This is followed by concluding remarks in section 4.

2. METHODOLOGY

2.1. Computational Details. All DFT calculations have been performed using the VASP code within the projector augmented wave (PAW) scheme,[58] employing the HSE06[47] range-separated hybrid exchange and correlation (xc)-functional. The geometries were taken from ref. 23, where they were fully relaxed using the PBE[39] xc-functional, with all forces $\lesssim 0.02$ eV/Å. To consider the effect of long-ranged van der Waals dispersion forces on the overlayer's structure and adsorption energy, we employ the vdW-DF[59–61] xc-functional based on PBE exchange. We employ a plane-wave energy cutoff of 445 eV, an electronic temperature $k_BT \approx 0.2$ eV with all energies extrapolated to $T \to 0$ K, that is, excluding the electronic entropy contribution to the free energy $-ST$, and a PAW pseudopotential for Ti that includes the $3s^2$ and $3p^6$ semi-core levels. The calculations have been performed spin unpolarized.

All unit cells contain a four layer TiO_2(110) slab, employ the measured lattice parameters of bulk rutile TiO_2 ($a = 4.5941$ Å, $c = 2.958$ Å),[62] and include at least 27 Å of vacuum between repeated images ($L_z = 50$ Å in [110] direction). For 1 and ⅔ monolayer (ML) catechol coverages, equivalent 1×4 and 1×3 catechol overlayers are adsorbed on both sides of the slab, yielding a total of four and two catechol molecules, respectively. We employ Γ centered 4×3×1 k-point meshes, with densities $\Delta k < 0.25$ Å^{-1}, and approximately 9¼ unoccupied bands per atom, that is, including all levels up to 30 eV above the valence band maximum (VBM).

For comparison, PBE G_0W_0 quasiparticle calculations have been performed based on the KS eigenvalues and wave functions from PBE DFT, as previously described in ref 23. The G_0W_0 parameters employed are consistent with those successfully used to describe both bulk rutile and anatase TiO_2, rutile TiO_2(110) and anatase TiO_2(101) clean surfaces, and their interfaces.[23,31–35]

We solve the Bethe-Salpeter equation using the KS eigenvalues and wave functions from HSE06 DFT as input, and a constant frequency-independent dielectric function ($\varepsilon_\infty \approx 4$). For the BSE calculations we have used 480 frequency sampling points, and included all the transitions from occupied HOMO and HOMO−1 levels to unoccupied levels with a maximum energy difference of 7 eV.[46] In so doing, the calculated spectra include absorption by the adsorbed dye, and transfer to conduction levels of the substrate.

For interfaces, the calculated intensities are inversely proportional to the unit cell parameter normal to the surface, that is, $I_\lambda \propto 1/L_z$. Since we employ the same unit cell parameter along the [110] direction for each catechol–TiO_2(110) structure, $L_z = 50$ Å, although the units of the computed intensities are necessarily arbitrary, they are the same for each of the four catechol–TiO_2(110) interfaces considered herein.

2.2. Terminology. Throughout the manuscript, the atomic orbitals of Ti are described in the octahedral basis, with x and y axes aligned with the Ti–O bonds, that is, according to O_h crystal field theory.[51] In this way, the atomic orbitals are grouped into those with t_{2g}-like symmetry, d_{xy}, d_{xz}, and d_{yz}, and those with e_g-like symmetry, $d_{x^2-y^2}$ and d_{z^2}.

Following the definitions of refs. 23 and 63, the adsorption energy per molecule of catechol E_{ads} on coordinately unsaturated Ti (Ti_{cus}) sites of a TiO_2(110) surface is given by

$$E_{ads} \approx \frac{E[N_{cat}C_6H_4(OH)_2 + TiO_2(110)] - E[TiO_2(110)]}{N_{cat}} - E[C_6H_4(OH)_2]. \quad (1)$$

Here N_{cat} is the number of adsorbed catechol molecules in the unit cell, and $E[N_{cat}C_6H_4(OH)_2 + TiO_2(110)]$, $E[TiO_2(110)]$, and $E[C_6H_4(OH)_2]$ are the total energies of the covered and clean surfaces and gas phase catechol molecule, respectively. We model catechol in the gas phase using the most stable conformation, which has an intramolecular hydrogen bond, that is, C_S symmetry.[23]

2.3. Density of States Alignment. Following the procedure laid out in ref. 23, we plot the DOS for catechol overlayers relative to the VBM of the clean surface $\varepsilon^{clean}_{VBM}$. This is accomplished by aligning the deepest Ti $3s^2$ semi-core levels for the clean and catechol covered TiO_2(110) surfaces, $\varepsilon^{clean}_{Ti3s^2}$ and ε_{Ti3s^2}, respectively. In this way, $\varepsilon_{VBM} = \varepsilon^{clean}_{VBM} - \varepsilon^{clean}_{Ti3s^2} + \varepsilon_{Ti3s^2}$. This allows us to directly compare the spectra of catechol overlayers as a function of coverage and deprotonation of the OH anchoring groups, that is, dissociation.[23]

2.4. Bethe-Salpter Equation. Assuming the KS wave functions ψ_n, with eigenenergies ε_n and occupations f_n, form an orthonormal and complete basis set, then in their electron-hole pair space, suppressing their k-point dependence, the four-point Bethe-Salpeter equation for the density-density response function χ is[37,45,46]

$$\chi_{SS'} = \chi^0_S\left[\delta_{nn'}\delta_{mm'} + \sum_{S''}[\mathcal{V}_{SS''} - \mathcal{W}_{SS''}]\chi_{S''S'}(\omega)\right] \quad (2)$$

where $m,m' \in \{1,\ldots,N_{occ}\}$, $n,n' \in \{N_{occ}+1,\ldots,N_{tot}\}$, N_{occ} is the number of occupied levels, N_{tot} is the total number of electronic levels included, $S \equiv \{m,n\}$, χ^0_{nm} is the non-interacting density-density response function

$$\chi^0_{nm} = \frac{f_m - f_n}{\omega - \varepsilon_n + \varepsilon_m}\delta_{nn'}\delta_{mm'} \quad (3)$$

$\mathcal{V}_{SS''}$ is the Coulomb interaction

$$\mathcal{V}_{SS''} = \int \mathrm{d}\mathbf{r}\mathrm{d}\mathbf{r}' \frac{\psi_m(\mathbf{r})\psi^*_n(\mathbf{r})\psi^*_{m''}(\mathbf{r}')\psi_{n''}(\mathbf{r}')}{\|\mathbf{r}-\mathbf{r}'\|} \quad (4)$$

and $\mathcal{W}_{SS''}$ is the static ($\omega = 0$) screening

$$\mathcal{W}_{SS''} = \int \mathrm{d}\mathbf{r}\mathrm{d}\mathbf{r}' \frac{\psi_m(\mathbf{r})\psi^*_n(\mathbf{r}')\epsilon^{-1}(\mathbf{r},\mathbf{r}';\omega=0)\psi^*_{m''}(\mathbf{r})\psi_{n''}(\mathbf{r}')}{\|\mathbf{r}-\mathbf{r}'\|} \quad (5)$$

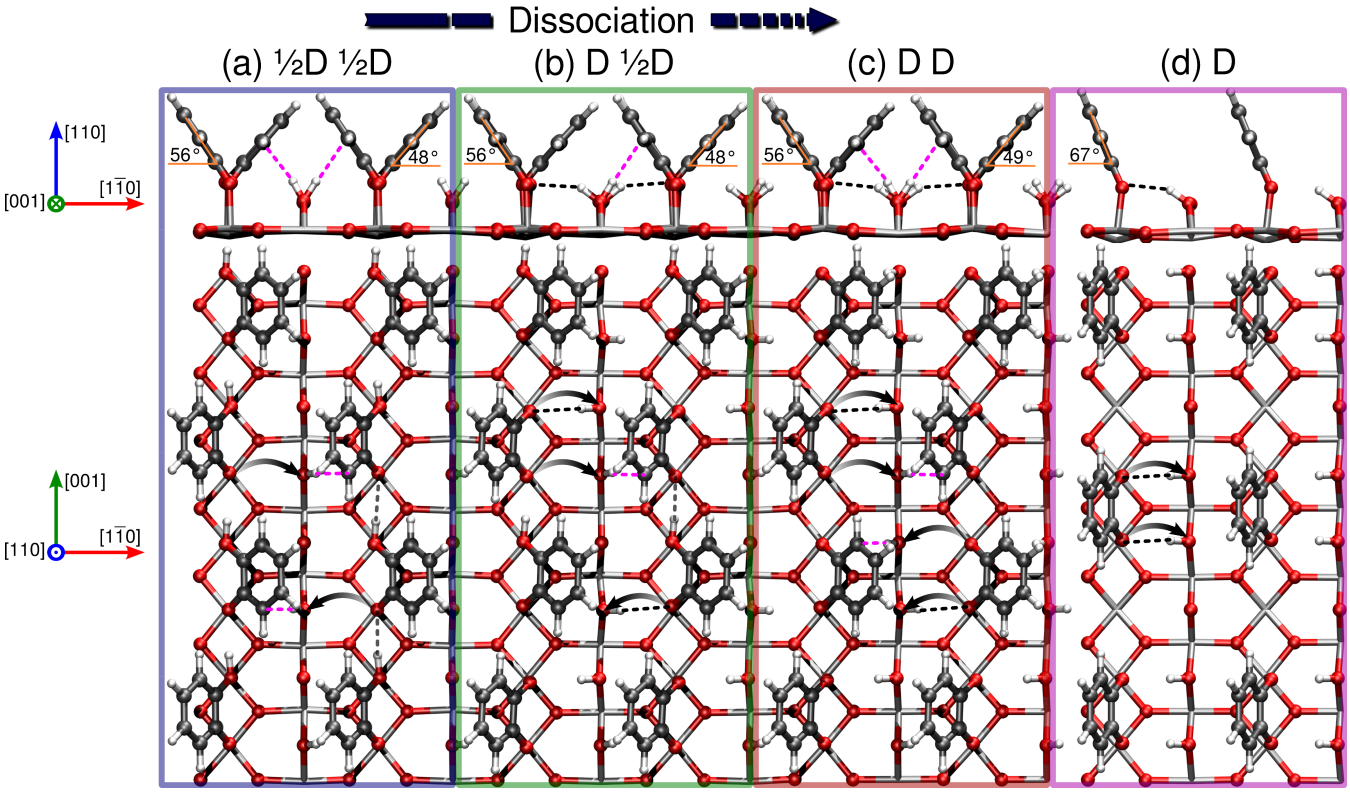

Figure 1. Schematics of 1 ML catechol adsorbed (a) half (½D ½D, blue), (b) mixed (D ½D, green), (c) fully (D D, red) dissociated and (d) ⅔ ML (violet) catechol adsorbed dissociated (D) on Ti_{cus} sites of TiO_2(110). Charge transfer of $\sim -0.4e$ accompanying deprotonation is represented by arrows, while intermolecular OH–O (gray) and interfacial O_{br}H–O (black) and O_{br}H–C (magenta) hydrogen bonds are denoted by dotted lines. The angle between catechol's benzene ring and the surface plane, θ, is shown above. Adapted with permission from ref. 23. Copyright 2015 American Chemical Society.

where $\epsilon^{-1}(\mathbf{r},\mathbf{r}';\omega)$ is approximated by a dielectric constant of four, that is, $\epsilon^{-1}(\mathbf{r},\mathbf{r}';\omega) \approx \epsilon_\infty^{-1} \approx 1/4$, within the range-separation of the hybrid xc-functional.

Substituting (3) into (2), we can reformulate (2) into an effective Hamiltonian eigenvalue problem

$$\mathcal{H}_{SS'} \equiv (\varepsilon_n - \varepsilon_m)\delta_{nn'}\delta_{mm'} - (f_n - f_m)[\mathcal{V}_{SS'} - \mathcal{W}_{SS'}] \quad (6)$$

with eigenvalues E_λ and eigenvectors A_λ^S from

$$\mathcal{H}_{SS'}A_\lambda^S = E_\lambda A_\lambda^S. \quad (7)$$

Here, E_λ and A_λ^S are the exciton energies and coefficients in electron-hole space. The λth exciton can then be expressed in terms of A_λ^S and ψ_n as

$$\Psi_\lambda(\mathbf{r}_e,\mathbf{r}_h) = \sum_{nm} A_\lambda^{nm}\psi_n(\mathbf{r}_e)\psi_m(\mathbf{r}_h) \quad (8)$$

where $\mathbf{r}_e$ and $\mathbf{r}_h$ are coordinates associated with the electron and hole, respectively.

To quantify the spatial distribution of the electron and hole of the λth exciton, it is convenient to invoke the electron and hole densities, $\rho_e(\mathbf{r}_e)$ and $\rho_h(\mathbf{r}_h)$, which are obtained by integrating (8) with respect to the hole and electron coordinates, respectively[64]

$$\begin{aligned}\rho_e(\mathbf{r}_e) &= \int d\mathbf{r}_h \Psi_\lambda(\mathbf{r}_e,\mathbf{r}_h)\Psi_\lambda^*(\mathbf{r}_e,\mathbf{r}_h) \\ &= \sum_{nm}\sum_{n'} A_\lambda^{nm}A_\lambda^{n'm^*}\psi_n(\mathbf{r}_e)\psi_{n'}^*(\mathbf{r}_e). \end{aligned} \quad (9)$$

Since

$$\int d\mathbf{r}_e A_\lambda^{nm}A_\lambda^{n'm^*}\psi_n(\mathbf{r}_e)\psi_{n'}^*(\mathbf{r}_e) = \left|A_\lambda^{nm}\right|^2\delta_{nn'} \quad (10)$$

and by construction

$$\sum_{nm}\left|A_\lambda^{nm}\right|^2 \equiv 1, \quad (11)$$

we ensure

$$\int d\mathbf{r}_e\rho_e(\mathbf{r}_e) = 1. \quad (12)$$

However, $A_\lambda^{nm}A_\lambda^{n'm^*}\psi_n(\mathbf{r}_e)\psi_{n'}^*(\mathbf{r}_e)$ is not necessarily zero for $n \neq n'$.

The exciton's electron/hole densities, $\rho_{e/h}(\mathbf{r}_{e/h})$, describe the spatial distribution of the electron/hole "averaged" over the hole/electron distribution. To differentiate between Frenkel[65] and Wannier[66] excitons, one would need to calculate the two-point excitonic wave function $\Psi_\lambda(\mathbf{r}_e,\mathbf{r}_h)$, fix the position of the electron or hole, and unfold the k-point dependent wave function into real space. More precisely, including explicitly the k-point dependence, Eq (8) becomes

$$\Psi_\lambda(\mathbf{r}_e,\mathbf{r}_h) = \sum_{\mathbf{k}}\sum_{nm} A_\lambda^{nm,\mathbf{k}}\psi_{n,\mathbf{k}}(\mathbf{r}_e)e^{i\mathbf{k}\cdot\mathbf{r}_e}\psi_{m,\mathbf{k}}(\mathbf{r}_h)e^{i\mathbf{k}\cdot\mathbf{r}_h}. \quad (13)$$

This would require a significantly larger k-point sampling to probe whether the excitonic wave functions decay over several nanometers. Further, the unit cells we have employed have too few layers to probe excitons with electron density in the bulk, and differentiate between bulk, surface, and bulk resonant levels. For these reasons, we focus herein on the exciton's electron and hole densities, $\rho_e(\mathbf{r}_e)$ and $\rho_h(\mathbf{r}_h)$, respectively.

3. RESULTS AND DISCUSSION

3.1. Overlayer Adsorption. We begin by considering the most stable catechol overlayers on TiO_2(110) from the literature.[23] Catechol consists of a benzene ring with two adjacent OH anchoring groups, which adsorbs on Ti_{cus} sites of the rutile TiO_2(110) sur-

face in a bidentate configuration.[20,23] From previous work,[20,23] we know from comparing STM, UPS, and IPES experiments to G_0W_0 and HSE06 DFT calculations that the interface has a 1 ML 1×4 coverage. We also consider the ⅔ ML 1×3 coverage to probe the dependence of the spectra on coverage and tilting of the molecule.

As shown in Figure 1, upon adsorption the OH anchoring groups may dissociate, that is, deprotonate, with a charge transfer of $\sim -0.4e$, indicated by arrows, accompanying the proton transfer to the adjacent bridging O atom (O_{br}) of the TiO_2(110) surface. At 1 ML coverage, besides interfacial hydrogen bonds from the surface's hydrogenated bridging oxygens (O_{br}H–C and O_{br}H–O), the overlayer, when not fully dissociated, is stabilized by intermolecular hydrogen bonds (OH–O) between neighboring catechol molecules, as depicted in Figure 1. For this reason, the 1 ML half (½D ½D), mixed (D ½D), and fully (D D) dissociated and ⅔ ML fully dissociated (D) catechol overlayers' adsorption energies are all within 0.1 eV, that is, the accuracy of DFT.[23,63]

In Table 1, we compare PBE DFT,[23,63] HSE06 DFT, and vdW-DF DFT adsorption energies for the most stable catechol overlayers on TiO_2(110). HSE06 DFT yields more stable absorption energies than PBE DFT by a constant shift of ~ 0.35 eV. The inclusion of van der Waals interactions (vdW-DF DFT) strengthens the adsorption energies for 1 ML catechol overlayers by a constant shift of ~ 1.58 eV relative to PBE DFT. However, at the lower ⅔ ML coverage where catechol is more upright ($\theta = 67°$), the van der Waals contribution to the adsorption energy is reduced by 0.2 eV, inverting the relative stabilities of the 1 ML and ⅔ ML coverages. This result is consistent with the experimental observation of 1 ML catechol overlayers on rutile TiO_2(110).[20,23] However, in all cases the adsorption energy per molecule is nearly isoenergetic for the half, mixed, fully dissociated 1 ML and dissociated ⅔ ML coverages. Furthermore, relaxation of the overlayer's structure at the vdW-DF DFT level leaves both the structure and adsorption energies unchanged up to the accuracy of DFT. This justifies our use of the PBE DFT geometries from ref 23.

Table 1. Adsorption Energies E_{ads} in Electronvolts from PBE,[23,63] HSE06, and vdW-DF DFT for 1 ML 1×4 and ⅔ ML 1×3 Half (½D) and Fully (D) Dissociated Catechol on TiO_2(110) with Tilting Angle θ in Degrees and Number of Intermolecular (OH–O) and Interfacial (O_{br}H–C and O_{br}H–O) Bonds per Unit Cell

structure	θ (deg.)	bonds/unit cell			E_{ads} (eV)		
		OH–O	O_{br}H–C	O_{br}H–O	PBE	HSE06	vdW-DF
1 ML ½D ½D	56, 49	2	2	0	−0.614[a]	−0.944	−2.176
1 ML D ½D	56, 48	1	1	2	−0.685[a]	−1.026	−2.273
1 ML D D	56, 49	0	2	2	−0.652[a]	−1.009	−2.228
⅔ ML D	67	0	0	2	−0.748[b]	−1.118	−2.128

[a]Reference 23. [b]Reference 63.

3.2. Interfacial Level Alignment. For catechol on TiO_2(110), the relevant levels for absorption of the solar spectrum are from catechol's mid-gap HOMO and HOMO−1[20,23] to the unoccupied Ti 3*d* levels with t_{2g}-like symmetry $\{d_{xy}, d_{xz}, d_{yz}\}$[50–52] of the substrate as the LUMO and LUMO+1 levels of catechol are significantly higher in energy.[23] In fact, intramolecular HOMO→LUMO transitions of the adsorbed molecular layer are significantly above the band gap of rutile TiO_2.[23]

An accurate description of the optical absorption spectra in the visible of the catechol–TiO_2(110) interface thus requires an accurate description of the interfacial level alignment of catechol's mid-gap HOMO and HOMO−1 and the unoccupied Ti 3*d* levels of the substrate. To quantify the accuracy of the calculated level alignment, one may compare the KS energy separation between catechol's HOMO and the substrate's CBM, $\Delta\varepsilon_{HOMO\rightarrow CBM} = \varepsilon_{CBM} - \varepsilon_{HOMO}$ with the binding energy of catechol's HOMO obtained from UPS experiments, as provided in Table 2. Since the measured Fermi level of rutile TiO_2 is approximately 0.1 eV below the CBM,[67–69] the energy separation between catechol's HOMO and the CBM of the TiO_2(110) surface from UPS measurements is $\Delta\varepsilon_{HOMO\rightarrow CBM} \approx 2.4 + 0.1 = 2.5$ eV.[20]

Table 2. HOMO→CBM KS Energy Differences $\Delta\varepsilon_{HOMO\rightarrow CBM}$, From PBE G_0W_0 and HSE06 DFT and the Lowest Energy Exciton's Energy $E_{(i)}$ and Binding Energy $E_b = E_{(i)} - \Delta\varepsilon_{HOMO\rightarrow CBM}$ in Electronvolts and Intensity $I_{(i)}$ From HSE06 BSE for 1 ML 1×4 and ⅔ ML 1×3 Half (½D) and Fully (D) Dissociated Catechol on TiO_2(110)

structure	$\Delta\varepsilon_{HOMO\rightarrow CBM}$ (eV)		$E_{(i)}$ (eV)	E_b (eV)	$I_{(i)}$
	PBE G_0W_0	HSE06 DFT		HSE06 BSE	
1 ML ½D ½D	3.926[a]	2.544	2.532	0.012	0.452
1 ML D ½D	3.441[a]	2.061	2.045	0.016	20.125
1 ML D D	3.307[a]	1.942	1.939	0.003	1.315
⅔ ML D	3.269	1.846	1.842	0.004	7.297
experiment	2.4[b]				

[a]Reference 23. [b]UPS binding energy relative to the Fermi level from ref 20.

As shown in Table 2, $\Delta\varepsilon_{HOMO\rightarrow CBM}$ from HSE06 DFT agrees semi-quantitatively with the binding energy measured with UPS for catechol on TiO_2(110).[20] Conversely, PBE G_0W_0 overestimates $\Delta\varepsilon_{HOMO\rightarrow CBM}$ by ~ 1 eV. This is consistent with the overestimation of the electronic gap for the TiO_2(110) surface by ~ 1 eV with PBE G_0W_0.[32] This motivates our use of HSE06 DFT eigenvalues as input to our BSE calculations.

In Figure 2, we compare the HSE06 DOS for the 1 ML half (½D ½D), mixed (D ½D), and fully (D D) dissociated and ⅔ ML dissociated (D) catechol on TiO_2(110). In each case, there are two distinct peaks outside the clean surface's VB region. These two peaks are associated with the HOMO−1 and HOMO levels of catechol.[23] As a reference, the HOMO of gas phase catechol, which has π character, is depicted in Figure 2.

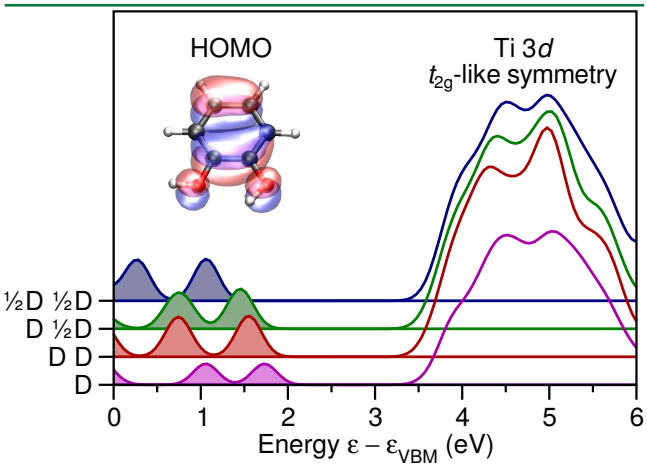

Figure 2. HSE06 DFT total DOS for 1 ML half (½D ½D, blue), mixed (D ½D, green), and fully (D D, red) dissociated and ⅔ ML fully (D, violet) dissociated catechol on TiO_2(110). Energies are relative to the VBM (ε_{VBM}) of clean TiO_2(110). Filling denotes occupation. The HOMO of isolated catechol is shown as an inset.

Figure 2 shows that the HOMO and HOMO−1 are pinned to each other, and shift up in energy with deprotonation of adsorbed catechol. This deprotonation of the OH anchoring group induces a charge transfer of $\sim -0.4e$ to the substrate. As charge is removed from the molecule, the HOMO and HOMO−1 are destabilized. This is because the molecule's ability to screen the HOMO and HOMO−1 levels is reduced as charge is transferred to the substrate.[31] Consequently, the energy separation between the HOMO and CBM, $\Delta\varepsilon_{HOMO\rightarrow CBM} = \varepsilon_{CBM} - \varepsilon_{HOMO}$, decreases with dissociation by ~ 0.6 eV, as provided in Table 2. Moreover, $\Delta\varepsilon_{HOMO\rightarrow CBM}$ decreases by a further 0.1 eV as the coverage decreases from 1 ML to ⅔ ML. This already suggests fully dissoci-

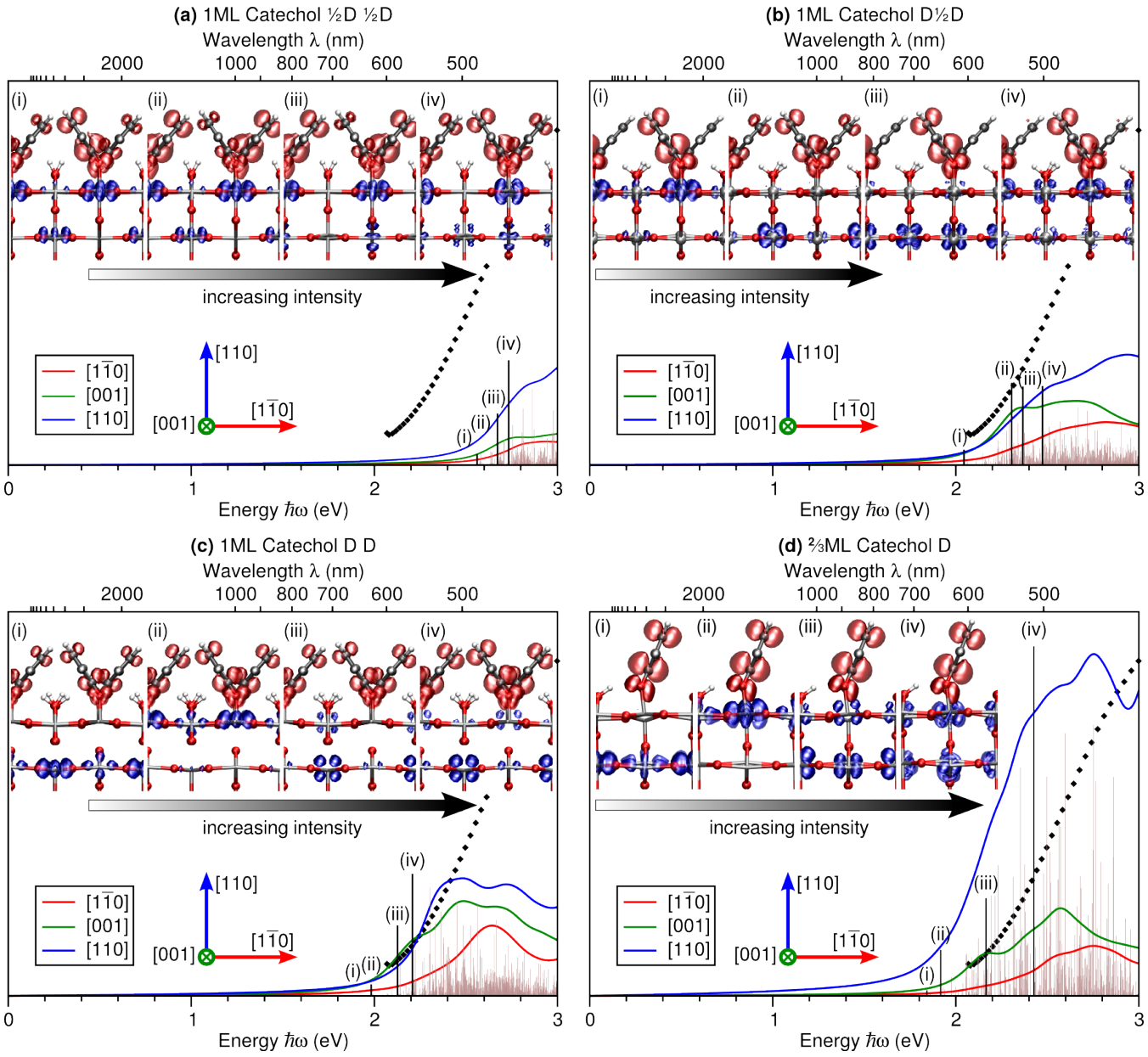

Figure 3. HSE06 BSE optical absorption spectra for light polarized along [1$\bar{1}$0] (red), [001] (green), and [110] (blue) directions of 1 ML **(a)** half (½D ½D), **(b)** mixed (D ½D), and **(c)** fully (D D) dissociated and **(d)** ⅔ ML fully dissociated catechol on TiO_2(110). Vertical lines denote the energies and intensities of individual excitons (brown). The electron (blue) and hole (red) densities, ρ_e and ρ_h, of four representative excitons (i–iv) chosen in order of increasing intensity with energy (black vertical lines) are shown as insets. Measured optical absorption of catechol on anatase TiO_2 nanoparticles (black diamonds) is taken from ref. 19.

ated catechol overlayers at lower coverage may have greater photovoltaic efficiencies.

3.3. Sub-Band Gap Optical Absorption. Optical absorption above the substrate band gap of 3.3 eV[70] will be dominated by supra-band gap transitions within the substrate. Here, we are focused on the photovoltaic efficiency of the dye-substrate interface. This means we may restrict consideration to sub-band gap transitions which are below the optical gap of rutile TiO_2 at 3.0 eV.[71,72] Moreover, these transitions are most relevant for absorption of solar irradiation.

For systems with weak electron-hole binding, the onset of the optical absorption spectra may already be well described within an independent-particle (IP) picture.[49,73] Further, excitons composed primarily of a single transition between KS levels would also be well described at the IP level. As shown in Figure S1 of the supporting information (SI), this is indeed the case for ⅔ ML D catechol on TiO_2(110), although significant differences in relative intensities with the BSE spectra are observed for catechol monolayers on TiO_2(110). However, the degree of electron-hole binding and mixing of the transitions that compose the relevant excitons is not known *a priori*. As a result, the reliability of the IP spectra can only be assessed after obtaining the BSE spectra.

In Figure 3 we show the angular resolved optical absorption spectra along the [1$\bar{1}$0], [001], and [110] directions for 1 ML ½D ½D, D ½D, D D, and ⅔ ML D catechol on TiO_2(110). We also show the spatial distribution of four representative excitons (i–iv) that have been chosen in order of increasing intensity with energy, as depicted schematically using arrows in Figure 3. The computed spectra include direct transitions from catechol's HOMO and HOMO−1 to the unoccupied Ti 3*d* conduction levels with t_{2g}-like

symmetry $\{d_{xy}, d_{xz}, d_{yz}\}$. The last N_{cat} occupied levels are bonding and antibonding levels composed of the HOMOs of the catechol molecules within our unit cells.[23] In Table 3 these are referred to as $m - N_{occ} = 0, -1, -2, -3$ and $m - N_{occ} = 0, -1$ for 1 ML 1×4 and ⅔ ML 1×3 catechol overlayers, respectively.

Table 3. Energy E_λ in Electronvolts, Intensity I_λ, and Transitions From Catechol's HOMO to TiO_2(110)'s CB $m \rightarrow n$ Relative to the Number of Occupied Levels N_{occ} at Given k-points with Amplitudes $|A_\lambda^{nm}|^2$ That Form the Four Excitons (i–iv) Shown in Figure 3 for 1 ML 1×4 ($m - N_{occ} = 0, -1, -2, -3$) and ⅔ ML 1×3 ($m - N_{occ} = 0, -1$) Half (½D) and Fully (D) Dissociated Catechol on TiO_2(110)

	exciton		transition		
λ	E_λ (eV)	I_λ (arb. units)	$m - N_{occ}$ $n - N_{occ} - 1$	k-point	$\lvert A_\lambda^{nm}\rvert^2$
			1 ML catechol ½D ½D		
(i)	2.532	0.452	−1 → 0, +2	Γ	68%
			0 → +1, +3	Γ	20%
(ii)	2.562	14.192	−2 → 0, +2	Γ	68%
			−3 → +1, +3	Γ	18%
(iii)	2.672	67.166	−3 → +3	Γ, ±⅔Y	15%
			−2 → +2	Γ, ±⅔Y	17%
			−3 → 0	±½X	10%
			0 → +1	±½X	6%
(iv)	2.734	136.457	−1 → +2	±½X	19%
			−3, −2 → +3	±⅔Y	17%
			1 ML catechol D ½D		
(i)	2.045	20.125	0 → 0, +3	Γ	53%
			−1 → +1, +2	Γ	30%
(ii)	2.305	107.222	0 → +1	±½X±⅔Y	51%
			−3 → +1	±⅔Y	12%
			0 → +2	±½X	7%
(iii)	2.366	102.162	0 → +5	±⅔Y	23%
			−1 → +5	Γ	11%
			0 → +4	±X	19%
			−1 → +5	±X	10%
(iv)	2.473	102.949	−1 → +7	±½X±⅔Y	34%
			0 → +10	±X±⅔Y	17%
			0 → +7	∓½X±⅔Y	5%
			0 → +8	±½X±⅔Y	4%
			1 ML catechol D D		
(i)	1.939	1.315	−1 → 0	Γ	95%
			0 → 0	Γ	4%
(ii)	1.983	14.925	0 → +1, +3	Γ	52%
			−1 → +2	Γ	31%
(iii)	2.127	91.871	−1 → +4	Γ	53%
			0 → +2	±X±⅔Y	8%
(iv)	2.208	158.836	−1, 0 → +4	±⅔Y	74%
			−1, 0 → +1	±½X±⅔Y	4%
			⅔ ML catechol D		
(i)	1.842	7.297	0 → 0	Γ	98%
(ii)	1.917	59.896	−1 → +2	Γ	42%
			−1 → +2	±⅔Y	2%
			0 → +3	Γ	37%
			0 → +3	±⅔Y	2%
(iii)	2.165	127.158	−1 → +4	Γ	54%
			0 → +6	Γ	10%
			0 → +4	±⅔Y	13%
(iv)	2.427	455.011	0 → +8	±⅔Y	90%

The individual KS transitions that form the four excitons (i–iv) shown in Figure 3 are provided in Table 3. As these are charge transfer excitations, one might expect BSE calculations to underestimate their intensity.[27,53–57] However, as shown in Figure 3 and Table 2, we find rather intense charge transfer excitons below 3 eV. Their hole density is localized on catechol's HOMO, while the electron density is composed of Ti $3d_{xy}$ orbitals. These transitions result in significant absorption in the visible region (400 – 700 nm) for the fully dissociated overlayers at ⅔ and 1 ML coverages. For half and mixed dissociated 1 ML overlayers, the HOMO and HOMO−1 are shifted lower in energy, resulting in a shift to higher energies of the absorption spectra. For 1 ML coverages, we find absorption along the [110] direction has similar intensities, while absorption in the surface plane increases in intensity with dissociation of the catechol overlayer (*cf.* Figure 3(a–c)).

Overall, our spectra for the catechol overlayers are consistent with that measured for colloidal catechol on anatase TiO_2 nanoparticles.[15,17–19] As shown in Figure 3, the measured spectrum has an onset at 600 nm, and a noticeable shoulder at 430 nm, in semi-quantitative agreement with our calculated optical absorption for catechol on rutile TiO_2(110). Moreover, taking into account the ~ 0.3 eV lower direct electronic band gap of rutile compared to anatase TiO_2,[35] the measured and calculated spectra would shift into near quantitative agreement for the most stable ⅔ ML catechol overlayer. This is consistent with the red shift of the absorption spectrum calculated with PBE time dependent (TD)DFT in ref. 16 for catechol on rutile compared to anatase TiO_2.

The spatial distribution of the lowest energy exciton, exciton (i), is shown for each catechol overlayer in Figure 3. For half ½D ½D and mixed D ½D dissociated catechol monolayers, exciton (i) has electron density located predominantly on surface Ti_{cus} sites, with some weight on subsurface Ti atoms, as shown in Figure 3(a) and (b), respectively. For fully dissociated 1 ML and ⅔ ML catechol overlayers, exciton (i) has electron density located almost entirely on subsurface Ti atoms, as shown in Figure 3(c) and (d). In each case, exciton (i) is composed of HOMO→CBM Ti $3d_{xy}$ transitions at Γ, as shown in Table 3. This suggests that fully deprotonating catechol's OH anchoring groups induces a larger spatial separation between the electron and hole normal to the surface. The binding of exciton (i) is quite weak, $\Delta\varepsilon_{HOMO\rightarrow CBM} - E_{(i)} \ll 25$ meV, as seen from Table 2. This means, at the BSE level, the onset of the spectra decreases with dissociation and reduction in coverage, due to the associated upshift of catechol's HOMO levels, shown in Figure 2.

Although the binding energies are very small (*cf.* Table 2), we find when the electron density is located on the surface Ti atoms (*cf.* Figure 3(a) and (b)), the binding energy is about four times greater than when the electron density is located on subsurface Ti atoms (*cf.* Figure 3(c) and (d)). This suggests, although electron and hole binding is greater when the electron density is located on the surface, separation of charge carriers is facile for catechol–TiO_2(110) interfaces.

The nature of the two different types of excitons with either smaller (*cf.* Figure 3(a) and (b)) or larger (*cf.* Figure 3(c) and (d)) separation normal to the surface between the charge carriers is in line with transient absorption spectra.[18] These indicate that back-electron transfer dynamics, that is, recovery time dynamics, are bi-exponential, with shorter and longer components. The fast component is in agreement with strong electronic coupling between charge carriers in these charge transfer states, and is attributed to the recovery time for electrons injected at Ti centers close to the adsorbate, e.g., Ti_{cus} sites. The slow component is attributed to the recovery time for electrons at a larger distance from the adsorbate. These results point to the important effect of charge separation on recovery time dynamics.[18,19]

From Table 2, we also find excitons (i) shown in Figure 3(b) and (d) are an order of magnitude more intense than those shown in Figure 3(a) and (c). More importantly, by reducing the coverage for fully dissociated catechol from 1 ML to ⅔ ML, absorption normal to the surface increases significantly in intensity, while absorption in the surface plane is somewhat reduced. This correlates with the catechol overlayer becoming more upright as the coverage is reduced (*cf.* Table 1), which should increase the dipole moment normal to the surface.

For the half dissociated ½D ½D catechol monolayer, the first two excitons, (i) and (ii), of Figure 3(a), are predominantly electronic transitions from HOMO→CBM at Γ (*cf.* Table 3). Exciton (i) has hole density mostly on the HOMO of the more upright molecule, while exciton (ii) has the hole density mostly on the HOMO of the more tilted molecule.[23] In both cases, the electron density is on the CBM, which has predominantly Ti_{cus} $3d_{xy}$ character, with some weight on the d_{xy} orbitals of the Ti atoms below O_{br} atoms.[35] Exciton (iii) has a hole density similar to exciton (ii), with the electron

density again having predominantly Ti_{cus} $3d_{xy}$ character, but with some weight on the d_{xy} orbitals of the Ti atoms below Ti_{cus} sites. The latter is attributable to the inclusion of transitions at other k-points (*cf.* Table 3). The hole density of exciton (iv) is a rather even mixture between the HOMOs of the two molecules, while the electron density of exciton (iv) is a mixture of d_{xy}, d_{xz}, and d_{yz} orbitals predominantly of Ti_{cus} sites, with some weight on the Ti atoms of the sub-layer. This exciton is composed of transitions at k-points away from Γ (*cf.* Table 3). The resulting Ti_{cus} $3d$ electron density yields a greater overlap with the O $2p_\pi$ levels of catechol's HOMO. This may explain exciton (iv)'s greater intensity.

For the mixed D ½D catechol monolayer, the hole density is predominantly on the more upright fully dissociated catechol molecules of the overlayer, as seen for excitons (i), (iii), and (iv) of Figure 3(b). Exciton (i) is predominantly a HOMO→CBM transition at Γ, with electron density mostly Ti_{cus} $3d_{xy}$ in character. The electron densities of excitons (ii) and (iii) are a mixture of d_{xz} and d_{yz} orbitals predominantly on subsurface Ti atoms. These excitons are mostly composed of transitions away from Γ (*cf.* Table 3). However, despite the significant spatial separation normal to the surface between the hole and electron densities which form excitons (ii) and (iii), their intensities are rather significant and similar. Exciton (iv), which has a similar intensity, has electron density predominantly on surface Ti atoms, with a mixed d_{xy}, d_{xz}, and d_{yz} character. This exciton is composed of transitions from HOMO to higher energy CB levels mostly in the middle of the Brillouin zone (*cf.* Table 3).

The fully dissociated catechol 1 ML and ⅔ ML overlayers have excitons (i–iv) with similar electron densities, as seen in Figure 3(c) and (d). For both coverages, exciton (i) is composed of HOMO→CBM transitions at Γ (*cf.* Table 3), with electron densities predominantly d_{xy} in character, on subsurface Ti atoms. Similarly, for both coverages, exciton (ii) is composed of transitions mostly at Γ from HOMO to higher energy CB levels (*cf.* Table 3), with electron densities predominantly d_{xy} in character, but on surface Ti atoms. For 1 ML, the electron densities of excitons (iii) and (iv) are a mixture of d_{xz} and d_{yz} orbitals predominantly on subsurface Ti atoms below O_{br}, with some weight on surface Ti atoms below O_{br} and Ti_{cus} sites, respectively. Exciton (iii) includes some transitions away from Γ, while the transitions of exciton (iv) are mostly away from Γ (*cf.* Table 3). For ⅔ ML, exciton (iii) and (iv) both have electron densities on Ti atoms throughout the substrate. While the electron density of exciton (iii), which includes transitions away from Γ, has a mixed d_{xz} and d_{yz} character, the electron density of exciton (iv) is a much more complex mixture of Ti $3d$ atomic orbitals, including a single transition from HOMO to a higher energy CB level away from Γ (*cf.* Table 3).

Overall, we find the brightest excitons tend to be composed of transitions away from Γ that have electron density on both surface and subsurface Ti atoms throughout the substrate. Excitons which are composed of a single transition at Γ are delocalized throughout the entire system, and do not decay. This is because the electron and hole densities are each composed of a single periodic KS orbital. In other words, such transitions are from the entire overlayer to the substrate. It is only when multiple transitions with differing phase factors, that is, away from Γ, are included that the electron and hole may be localized and decay through destructive interference between the KS wave functions. In this way the exciton may have the hole located on, e.g., the O $2p_\pi$ orbital of a single catechol molecule, with the electron density decaying into the substrate.

This may be important for excitons composed of transitions away from Γ, such as exciton (iv) of Figure 3(d). This exciton's squared planar averaged excitonic wave function in the [001] direction, $\iint |\Psi_\lambda(\mathbf{r}_e,\mathbf{r}_h)|^2 dS$, is shown in Figure 4. Here, the calculated Bloch wave function, with three k-points in the [001] direction, has been

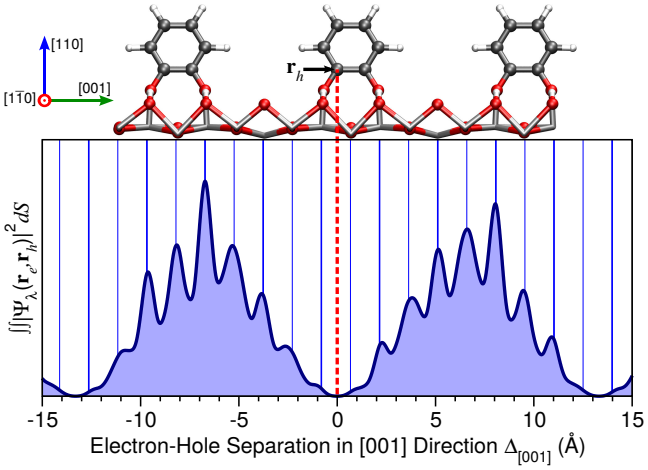

Figure 4. Squared planar averaged excitonic wave function $\iint |\Psi_\lambda(\mathbf{r}_e,\mathbf{r}_h)|^2 dS$ versus electron-hole separation in the [001] direction $\Delta_{[001]}$ in Å, fixing the hole position (red vertical dashed line) at the maximum of the hole density, $\max_{\mathbf{r}_h} \rho_h(\mathbf{r}_h)$, for exciton (iv) of the fully dissociated ⅔ ML catechol on TiO_2(110) shown in Figure 3(d). The positions of Ti atoms, Ti_{cus} and Ti–O_{br}, are denoted by blue vertical lines, thick and thin, respectively.

unfolded into real space. This representation of Ψ_λ has by construction a periodicity of 26.622 Å in the [001] direction. Increasing the number of k-points in the [001] direction would remove this constraint, potentially removing the nodes in the excitonic wave function at $\Delta_{[001]} \approx \pm 13.311$ Å in Figure 4. We have fixed the hole position $\mathbf{r}_h$ to the maximum of the hole density ρ_h, which is on the outer p lobe of a C atom bonding to the anchoring O atom, as shown in Figure 4.

We clearly see from Figure 4, that although exciton (iv) for the fully dissociated ⅔ ML catechol overlayer is very intense (*cf.* Figure 3(d)), the electron and hole are spatially separate. Moreover, the majority of the electron density is on Ti atoms below a catechol molecule adjacent to that on which the hole is located. This means exciton (iv) of Figure 3(d) is a charge transfer transition in both the [001] and [110] directions. This suggests electron-hole separation should be facile for this bright exciton.

4. CONCLUSIONS

We have performed HSE06-based BSE calculations of the optical absorption spectra and bright excitons for the most stable catechol overlayers on rutile TiO_2(110) as a function of coverage and dissociation. The catechol–TiO_2(110) interface is a type-II DSSC, with charge transfer transitions from the HOMO of catechol directly to the CB Ti $3d$ levels of the TiO_2 substrate. Our calculated spectra agree semi-quantitatively with the measured spectra for catechol on anatase TiO_2 nanoparticles. However, our results, combined with the lower direct electronic band gap of bulk rutile compared to anatase TiO_2,[35] suggest that the absorption spectra of catechol on rutile TiO_2(110) has a better overlap with the visible region of the solar spectra than catechol on anatase TiO_2 nanoparticles. Thus, the catechol–TiO_2(110) interface may provide a greater photovoltaic efficiency than catechol on anatase TiO_2 nanoparticles. This provides motivation for future experimental studies of the optical absorption of the catechol–TiO_2(110) interface.

The computation of the absorption spectra, excitonic binding energies, and spatial distribution of the excitons provides valuable information for discussing how facile charge transfer and electron-hole separation is in type-II DSSCs. As the catechol overlayer is dissociated, the onset of the absorption spectrum shifts to lower

energies. The lowest-energy excitons are rather bright, with low binding energies, and consist of charge transfer transitions from the overlayer's HOMO to the substrate's CBM. In agreement with transient absorption spectra [18] we find that these excitons have different degrees of charge separation onto either surface or subsurface Ti atoms.

The relationship between intensity and charge transfer is rather complex, and one must consider the directional dependence of the absorption spectra. Absorption along the [110] direction is related to charge transfer from the catechol overlayer to the substrate, while absorption along the [001] direction is related to charge transfer to adjacent catechol adsorption sites. For all structures we find the strongest absorption is in the [110] direction.

The ⅔ ML catechol overlayer has a significantly stronger absorption normal to the surface plane than the 1 ML catechol overlayers. The brightest exciton for fully dissociated ⅔ ML catechol on TiO_2(110) is a charge transfer transition with the electron and hole spatially separated in both the [110] and [001] directions. This suggests electron conduction is most probably via a superposition of d_{xz} and d_{yz} orbitals aligned in the [1$\bar{1}$0] direction.

Overall, our results suggest the excitons of the catechol–TiO_2(110) interface are spread out over several unit cells. This is based on their weak binding energies, the lower energy excitons being predominantly composed of transitions at Γ, and the weak dispersion of rutile TiO_2's band structure. Such excitons would be difficult to describe with small nanoparticle models for the substrate. This work motivates future calculations with denser k-point meshes and thicker substrate models to determine whether the bright excitons of the catechol–TiO_2 interface have Frenkel or Wannier character.

ASSOCIATED CONTENT

Supporting Information

The Supporting Information is available free of charge on the ACS Publications website at DOI: 10.1021/acs.jctc.6b00217.

Comparison of IP and BSE optical absorption spectra, total energies, and atomic coordinates of all structures (PDF)

AUTHOR INFORMATION

Corresponding Author

*E-mail: duncan.mowbray@gmail.com.

*E-mail: annapaola.migani@icn2.cat.

Notes

The authors declare no competing financial interest.

ACKNOWLEDGMENTS

We acknowledge financial support from Spanish Grants (FIS2012-37549-C05-02, FIS2013-46159-C3-1-P, RYC-2011-09582, JCI-2010-08156); Generalitat de Catalunya (2014SGR301, XRQTC); Grupos Consolidados UPV/EHU del Gobierno Vasco (IT-578-13).

REFERENCES

(1) Grätzel, M. Photoelectrochemical Cells. *Nature* **2001**, *414*, 338–344.

(2) U. S. Department of Energy. Photovoltaic Cell Conversion Efficiency Basics. http://energy.gov/eere/energybasics/articles/photovoltaic-cell-conversion-efficiency-basics (accessed Aug 20, 2013).

(3) Marom, N.; Körzdörfer, T.; Ren, X.; Tkatchenko, A.; Chelikowsky, J. R. Size Effects in the Interface Level Alignment of Dye-Sensitized TiO_2 Clusters. *J. Phys. Chem. Lett.* **2014**, *5*, 2395–2401.

(4) Planells, M.; Pelleja, L.; Clifford, J. N.; Pastore, M.; De Angelis, F.; Lopez, N.; Marder, S. R.; Palomares, E. Energy Levels, Charge Injection, Charge Recombination and Dye Regeneration Dynamics for Donor-Acceptor π-Conjugated Organic Dyes in Mesoscopic TiO_2 Sensitized Solar Cells. *Energy Environ. Sci.* **2011**, *4*, 1820–1829.

(5) Calzolari, A.; Ruini, A.; Catellani, A. Anchor Group versus Conjugation: Toward the Gap-State Engineering of Functionalized ZnO(10$\bar{1}$0) Surface for Optoelectronic Applications. *J. Am. Chem. Soc.* **2011**, *133*, 5893–5899.

(6) Labat, F.; Bahers, T. L.; Ciofini, I.; Adamo, C. First-Principles Modeling of Dye-Sensitized Solar Cells: Challenges and Perspectives. *Acc. Chem. Res.* **2012**, *45*, 1268–1277.

(7) Bahers, T. L.; Pauporté, T.; Lainé, P. P.; Labat, F.; Adamo, C.; Ciofini, I. Modeling Dye-Sensitized Solar Cells: From Theory to Experiment. *J. Phys. Chem. Lett.* **2013**, *4*, 1044–1050.

(8) Kandada, A. R. S.; Fantacci, S.; Guarnera, S.; Polli, D.; Lanzani, G.; Angelis, F. D.; Petrozza, A. Role of Hot Singlet Excited States in Charge Generation at the Black Dye/TiO_2 Interface. *ACS Appl. Mater. Interfaces* **2013**, *5*, 4334–4339.

(9) De Angelis, F.; Di Valentin, C.; Fantacci, S.; Vittadini, A.; Selloni, A. Theoretical Studies on Anatase and Less Common TiO_2 Phases: Bulk, Surfaces, and Nanomaterials. *Chem. Rev.* **2014**, *114*, 9708–9753.

(10) Lasser, L.; Ronca, E.; Pastore, M.; Angelis, F. D.; Cornil, J.; Lazzaroni, R.; Beljonne, D. Energy Level Alignment at Titanium Oxide–Dye Interfaces: Implications for Electron Injection and Light Harvesting. *J. Phys. Chem. C* **2015**, *119*, 9899–9909.

(11) Pratik, S. M.; Datta, A. Computational design of concomitant type-I and type-II porphyrin sensitized solar cells. *Phys. Chem. Chem. Phys.* **2013**, *15*, 18471–18481.

(12) An, B.-K.; Hu, W.; Burn, P. L.; Meredith, P. New Type II Catechol-Thiophene Sensitizers for Dye-Sensitized Solar Cells. *J. Phys. Chem. C* **2010**, *114*, 17964–17974.

(13) Ooyama, Y.; Harima, Y. Photophysical and Electrochemical Properties, and Molecular Structures of Organic Dyes for Dye-Sensitized Solar Cells. *ChemPhysChem* **2012**, *13*, 4032–4080.

(14) Persson, P.; Bergström, R.; Lunell, S. Quantum Chemical Study of Photoinjection Processes in Dye-Sensitized TiO_2 Nanoparticles. *J. Phys. Chem. B* **2000**, *104*, 10348–10351.

(15) Zhang, G.; Kim, G.; Choi, W. Visible Light Driven Photocatalysis Mediated via Ligand-to-Metal Charge Transfer (LMCT): An Alternative Approach to Solar Activation of Titania. *Energy Environ. Sci.* **2014**, *7*, 954–966.

(16) Lin, H.; Fratesi, G.; Selçuk, S.; Brivio, G. P.; Selloni, A. Effects of Thermal Fluctuations on the Structure, Level Alignment, and Absorption Spectrum of Dye-Sensitized TiO_2: A Comparative Study of Catechol and Isonicotinic Acid on the Anatase (101) and Rutile (110) Surfaces. *J. Phys. Chem. C* **2016**, *120*, 3899–3905.

(17) Moser, J.; Punchihewa, S.; Infelta, P. P.; Graetzel, M. Surface Complexation of Colloidal Semiconductors Strongly Enhances Interfacial Electron-Transfer Rates. *Langmuir* **1991**, *7*, 3012–3018.

(18) Wang, Y.; Hang, K.; Anderson, N. A.; ; Lian, T. Comparison of Electron Transfer Dynamics in Molecule-to-Nanoparticle and Intramolecular Charge Transfer Complexes. *J. Phys. Chem. B* **2003**, *107*, 9434–9440.

(19) Kaniyankandy, S.; Rawalekar, S.; Sen, A.; Ganguly, B.; Ghosh, H. N. Does Bridging Geometry Influence Interfacial Electron Transfer Dynamics? Case of the Enediol-TiO_2 System. *J. Phys. Chem. C* **2012**, *116*, 98–103.

(20) Li, S.-C.; Wang, J.-g.; Jacobson, P.; Gong, X.-Q.; Selloni, A.; Diebold, U. Correlation between Bonding Geometry and Band Gap States at Organic–Inorganic Interfaces: Catechol on Rutile TiO_2(110). *J. Am. Chem. Soc.* **2009**, *131*, 980–984.

(21) Risplendi, F.; Cicero, G.; Mallia, G.; Harrison, N. M. A Quantum-Mechanical Study of the Adsorption of Prototype Dye Molecules on Rutile-TiO_2(110): A Comparison between Catechol and Isonicotinic Acid. *Phys. Chem. Chem. Phys.* **2013**, *15*, 235–243.

(22) Duncan, W. R.; Prezhdo, O. V. Theoretical Studies of Photoinduced Electron Transfer in Dye-Sensitized TiO_2. *Annu. Rev. Phys. Chem.* **2007**, *58*, 143–184.

(23) Mowbray, D. J.; Migani, A. Using G_0W_0 Level Alignment to Identify Catechol's Structure on TiO_2(110). *J. Phys. Chem. C* **2015**, *119*, 19634–19641.

(24) Li, S.-C.; Chu, L.-N.; Gong, X.-Q.; Diebold, U. Hydrogen Bonding Controls the Dynamics of Catechol Adsorbed on a TiO_2(110) Surface. *Science* **2010**, *328*, 882–884.

(25) Duncan, W. R.; Prezhdo, O. V. Electronic Structure and Spectra of Catechol and Alizarin in the Gas Phase and Attached to Titanium. *J. Phys. Chem. B* **2005**, *109*, 365–373.

(26) Liu, L.-M.; Li, S.-C.; Cheng, H.; Diebold, U.; Selloni, A. Growth and Organization of an Organic Molecular Monolayer on TiO_2: Catechol on Anatase (101). *J. Am. Chem. Soc.* **2011**, *133*, 7816–7823.

(27) Varaganti, S.; Ramakrishna, G. Dynamics of Interfacial Charge Transfer Emission in Small Molecule Sensitized TiO_2 Nanoparticles: Is It Localized or Delocalized? *J. Phys. Chem. C* **2010**, *114*, 13917–13925.

(28) Zhang, L.; Cole, J. M. Anchoring Groups for Dye-Sensitized Solar Cells. *ACS Appl. Mater. Interfaces* **2015**, *7*, 3427–3455.

(29) Rangan, S.; Theisen, J.-P.; Bersch, E.; Bartynski, R. Energy Level Alignment of Catechol Molecular Orbitals on ZnO(110) and TiO_2(110) Surfaces. *Appl. Surf. Sci.* **2010**, *256*, 4829–4833.

(30) Rego, L. G. C.; ; Batista, V. S. Quantum Dynamics Simulations of Interfacial Electron Transfer in Sensitized TiO_2 Semiconductors. *J. Am. Chem. Soc.* **2003**, *125*, 7989–7997.

(31) Migani, A.; Mowbray, D. J.; Iacomino, A.; Zhao, J.; Petek, H.; Rubio, A. Level Alignment of a Prototypical Photocatalytic System: Methanol on TiO_2(110). *J. Am. Chem. Soc.* **2013**, *135*, 11429–11432.

(32) Migani, A.; Mowbray, D. J.; Zhao, J.; Petek, H.; Rubio, A. Quasiparticle Level Alignment for Photocatalytic Interfaces. *J. Chem. Theory Comput.* **2014**, *10*, 2103–2114.

(33) Migani, A.; Mowbray, D. J. Coverage Dependence of the Level Alignment for Methanol on TiO_2(110). *Comput. Theor. Chem.* **2014**, *1040–1041*, 259–265.

(34) Migani, A.; Mowbray, D. J.; Zhao, J.; Petek, H. Quasiparticle Interfacial Level Alignment of Highly Hybridized Frontier Levels: H_2O on TiO_2(110). *J. Chem. Theory Comput.* **2015**, *11*, 239–251.

(35) Sun, H.; Mowbray, D. J.; Migani, A.; Zhao, J.; Petek, H.; Rubio, A. Comparing Quasiparticle H_2O Level Alignment on Anatase and Rutile TiO_2. *ACS Catal.* **2015**, *5*, 4242–4254.

(36) Hedin, L. New Method for Calculating the One-Particle Green's Function with Application to the Electron-Gas Problem. *Phys. Rev.* **1965**, *139*, A796–A823.

(37) Onida, G.; Reining, L.; Rubio, A. Electronic Excitations: Density-Functional versus Many-Body Green's-Function Approaches. *Rev. Mod. Phys.* **2002**, *74*, 601–659.

(38) Shishkin, M.; Kresse, G. Implementation and Performance of the Frequency-Dependent *GW* Method within the PAW Framework. *Phys. Rev. B: Condens. Matter Mater. Phys.* **2006**, *74*, 035101.

(39) Perdew, J. P.; Burke, K.; Ernzerhof, M. Generalized Gradient Approximation Made Simple. *Phys. Rev. Lett.* **1996**, *77*, 3865.

(40) Brookes, I. M.; Muryn, C. A.; Thornton, G. Imaging Water Dissociation on TiO_2(110). *Phys. Rev. Lett.* **2001**, *87*, 266103.

(41) Kurtz, R. L.; Stock-Bauer, R.; Madey, T. E.; Román, E.; De Segovia, J. L. Synchrotron Radiation Studies of H_2O Adsorption on TiO_2(110). *Surf. Sci.* **1989**, *218*, 178–200.

(42) Krischok, S.; Höfft, O.; Günster, J.; Stultz, J.; Goodman, D.; Kempter, V. H_2O Interaction with Bare and Li-Precovered TiO_2: Studies with Electron Spectroscopies (MIES and UPS(HeI and II)). *Surf. Sci.* **2001**, *495*, 8–18.

(43) Wang, L.-Q.; Ferris, K. F.; Winokur, J. P.; Shultz, A. N.; Baer, D. R.; Engelhard, M. H. Interactions of Methanol with Stoichiometric and Defective TiO_2(110) and (100) surfaces. *J. Vac. Sci. Tech. A* **1998**, *16*, 3034–3040.

(44) Onda, K.; Li, B.; Zhao, J.; Petek, H. The Electronic Structure of Methanol Covered TiO_2(110) Surfaces. *Surf. Sci.* **2005**, *593*, 32–37.

(45) Salpeter, E. E.; Bethe, H. A. A Relativistic Equation for Bound-State Problems. *Phys. Rev.* **1951**, *84*, 1232–1242.

(46) van Setten, M. J.; Gremaud, R.; Brocks, G.; Dam, B.; Kresse, G.; de Wijs, G. A. Optical Response of the Sodium Alanate System: GW_0-BSE Calculations and Thin Film Measurements. *Phys. Rev. B: Condens. Matter Mater. Phys.* **2011**, *83*, 035422.

(47) Krukau, A. V.; Vydrov, O. A.; Izmaylov, A. F.; Scuseria, G. E. Influence of the Exchange Screening Parameter on the Performance of Screened Hybrid Functionals. *J. Chem. Phys.* **2006**, *125*, 224106.

(48) Paier, J.; Asahi, R.; Nagoya, A.; Kresse, G. Cu_2ZnSnS_4 as a Potential Photovoltaic Material: A Hybrid Hartree-Fock Density Functional Theory Study. *Phys. Rev. B: Condens. Matter Mater. Phys.* **2009**, *79*, 115126.

(49) Paier, J.; Marsman, M.; Kresse, G. Dielectric Properties and Excitons for Extended Systems from Hybrid Functionals. *Phys. Rev. B: Condens. Matter Mater. Phys.* **2008**, *78*, 121201.

(50) Mowbray, D. J.; Martínez, J. I.; Calle-Vallejo, F.; Rossmeisl, J.; Thygesen, K. S.; Jacobsen, K. W.; Nørskov, J. K. Trends in Metal Oxide Stability for Nanorods, Nanotubes, and Surfaces. *J. Phys. Chem. C* **2011**, *115*, 2244–2252.

(51) Wang, Z. *et al.* Localized Excitation of Ti^{3+} Ions in the Photoabsorption and Photocatalytic Activity of Reduced Rutile TiO_2. *J. Am. Chem. Soc.* **2015**, *137*, 9146–9152.

(52) Argondizzo, A.; Cui, X.; Wang, C.; Sun, H.; Shang, H.; Zhao, J.; Petek, H. Ultrafast Multiphoton Pump-Probe Photoemission Excitation Pathways in Rutile TiO_2(110). *Phys. Rev. B: Condens. Matter Mater. Phys.* **2015**, *91*, 155429.

(53) Dreuw, A.; Weisman, J. L.; Head-Gordon, M. Long-Range Charge-Transfer Excited States in Time-Dependent Density Functional Theory Require Non-Local Exchange. *J. Chem. Phys.* **2003**, *119*, 2943–2946.

(54) Berardo, E.; Hu, H.-S.; van Dam, H. J. J.; Shevlin, S. A.; Woodley, S. M.; Kowalski, K.; Zwijnenburg, M. A. Describing Excited State Relaxation and Localization in TiO_2 Nanoparticles Using TD-DFT. *J. Chem. Theory Comput.* **2014**, *10*, 5538–5548.

(55) Berardo, E.; Hu, H.-S.; Shevlin, S. A.; Woodley, S. M.; Kowalski, K.; Zwijnenburg, M. A. Modeling Excited States in TiO_2 Nanoparticles: On the Accuracy of a TD-DFT Based Description. *J. Chem. Theory Comput.* **2014**, *10*, 1189–1199.

(56) Nunzi, F.; Agrawal, S.; Selloni, A.; Angelis, F. D. Structural and Electronic Properties of Photoexcited TiO_2 Nanoparticles from First Principles. *J. Chem. Theory Comput.* **2015**, *11*, 635–645.

(57) Kronik, L.; Stein, T.; Refaely-Abramson, S.; Baer, R. Excitation Gaps of Finite-Sized Systems from Optimally Tuned Range-Separated Hybrid Functionals. *J. Chem. Theory Comput.* **2012**, *8*, 1515–1531.

(58) Kresse, G.; Joubert, D. From Ultrasoft Pseudopotentials to the Projector Augmented-Wave Method. *Phys. Rev. B: Condens. Matter Mater. Phys.* **1999**, *59*, 1758.

(59) Dion, M.; Rydberg, H.; Schröder, E.; Langreth, D. C.; Lundqvist, B. I. Van der Waals Density Functional for General Geometries. *Phys. Rev. Lett.* **2004**, *92*, 246401.

(60) Román-Pérez, G.; Soler, J. M. Efficient Implementation of a van der Waals Density Functional: Application to Double-Wall Carbon Nanotubes. *Phys. Rev. Lett.* **2009**, *103*, 096102.

(61) Klimeš, J.; Bowler, D. R.; Michaelides, A. Van der Waals density functionals applied to solids. *Phys. Rev. B: Condens. Matter Mater. Phys.* **2011**, *83*, 195131.

(62) Burdett, J. K.; Hughbanks, T.; Miller, G. J.; Richardson, J. W.; Smith, J. V. Structural-Electronic Relationships in Inorganic Solids: Powder Neutron Diffraction Studies of the Rutile and Anatase Polymorphs of Titanium Dioxide at 15 and 295 K. *J. Am. Chem. Soc.* **1987**, *109*, 3639–3646.

(63) Mowbray, D. J.; Migani, A. Correction to "Using G_0W_0 Level Alignment to Identify Catechol's Structure on TiO_2(110)". *J. Phys. Chem. C* **2016**, *120*, 4151–4151.

(64) Glanzmann, L. N.; Mowbray, D. J.; Rubio, A. PFO-BPy Solubilizers for SWNTs: Modelling Polymers from Oligomers. *Phys. Stat. Solidi B* **2014**, *251*, 2407–2412.

(65) Frenkel, J. On the Transformation of Light into Heat in Solids. I. *Phys. Rev.* **1931**, *37*, 17–44.

(66) Wannier, G. H. The Structure of Electronic Excitation Levels in Insulating Crystals. *Phys. Rev.* **1937**, *52*, 191–197.

(67) Sato, N. *Electrochemistry at Metal and Semiconductor Electrodes*; Elsivier Science & Technology: Oxford, 1998.

(68) Aono, M.; Hasiguti, R. R. Interaction and Ordering of Lattice Defects in Oxygen-Deficient Rutile TiO_{2-x}. *Phys. Rev. B: Condens. Matter Mater. Phys.* **1993**, *48*, 12406–12414.

(69) Yamakata, A.; Ishibashi, T.; Onishi, H. Kinetics of the Photocatalytic Water-Splitting Reaction on TiO_2 and Pt/TiO_2 Studied by Time-Resolved Infrared Absorption Spectroscopy. *J. Mol. Catal. A: Chem.* **2003**, *199*, 85–94.

(70) Tezuka, Y.; Shin, S.; Ishii, T.; Ejima, T.; Suzuki, S.; Sato, S. Photoemission and Bremsstrahlung Isochromat Spectroscopy Studies of TiO_2 (Rutile) and $SrTiO_3$. *J. Phys. Soc. Jpn.* **1994**, *63*, 347–357.

(71) Amtout, A.; Leonelli, R. Optical Properties of Rutile Near its Fundamental Band Gap. *Phys. Rev. B: Condens. Matter Mater. Phys.* **1995**, *51*, 6842–6851.

(72) Pascual, J.; Camassel, J.; Mathieu, H. Fine Structure in the Intrinsic Absorption Edge of TiO_2. *Phys. Rev. B: Condens. Matter Mater. Phys.* **1978**, *18*, 5606–5614.

(73) Glanzmann, L. N.; Mowbray, D. J.; Figueroa del Valle, D. G.; Scotognella, F.; Lanzani, G.; Rubio, A. Photoinduced Absorption within Single-Walled Carbon Nanotube Systems. *J. Phys. Chem. C* **2015**, *120*, 1926–1935.